The sodium exosphere of Mercury: Comparison between observations during Mercury's transit and model results

Alessandro Mura, Peter Wurz, Herbert I.M. Lichtenegger, Helmold Schleicher, Helmut Lammer, Dominique C. Delcourt, Anna Milillo, Stefano Orsini, Stefano Massetti, Maxim L. Khodachenko

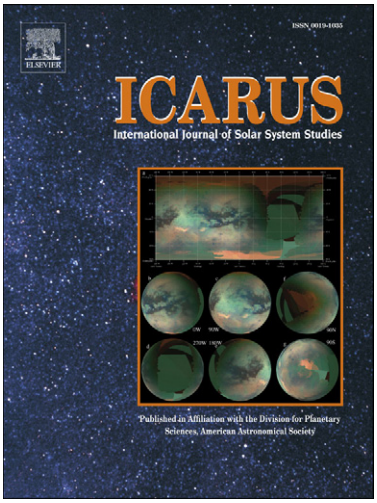

The sodium exosphere of Mercury: Comparison between observations during Mercury's transit and model results

Alessandro Mura, Peter Wurz, Herbert I.M. Lichtenegger, Helmold Schleicher, Helmut Lammer, Dominique Delcourt, Anna Milillo, Stefano Orsini, Stefano Massetti, Maxim L. Khodachenko

PII: S0019-1035(08)00410-7
DOI: 10.1016/j.icarus.2008.11.014
Reference: YICAR 8820

To appear in: *Icarus*

Received date: 29 April 2008
Revised date: 23 October 2008
Accepted date: 10 November 2008

Please cite this article as: A. Mura, P. Wurz, H.I.M. Lichtenegger, H. Schleicher, H. Lammer, D. Delcourt, A. Milillo, S. Orsini, S. Massetti, M.L. Khodachenko, The sodium exosphere of Mercury: Comparison between observations during Mercury's transit and model results, *Icarus* (2008), doi: 10.1016/j.icarus.2008.11.014

The sodium exosphere of Mercury: Comparison between observations during Mercury's transit and model results

Alessandro Mura[a], Peter Wurz[b], Herbert I.M. Lichtenegger[c], Helmold Schleicher[d], Helmut Lammer[c], Dominique Delcourt[e], Anna Milillo[a], Stefano Orsini[a], Stefano Massetti[a], Maxim L. Khodachenko[c]

[a] Istituto di Fisica dello Spazio Interplanetario-CNR, Rome, Italy

[b] Physics Institute, University of Bern, Bern, Switzerland

[c] Space Research Institute, Austrian Academy of Sciences, Graz, Austria

[d] Kiepenheuer-Institut fuer Sonnenphysik, Freiburg, Germany

[e] CETP-CNRS, Saint Maurice des Fossés, France

Proposed Running Head: The sodium exosphere of Mercury

Editorial correspondence to:

Dr. Alessandro Mura

Institute of Interplanetary Space Physics

INAF-IFSI Rome

Email: alessandro.mura@ifsi-roma.inaf.it

Key Words: Mercury transit, sodium exosphere, surface release processes, chemical sputtering

ABSTRACT-

In this study we compare the sodium exosphere observations made by Schleicher et al.(2004) with the result of a detailed numerical simulation. The observations, made during the transit of Mercury across the solar disk on 7 May 2003, show a maximum of sodium emission near the polar regions, with north prevalence, and the presence of a dawn-dusk asymmetry. We interpret this distribution as the resulting effect of two combined processes: the solar wind proton precipitation causing chemical alteration of the surface, freeing the sodium atoms from their bounds in the crystalline structure on the surface, and the subsequent photon-stimulated and thermal desorption of the sodium atoms. While we find that the velocity distribution of photon desorbed sodium can explain the observed exosphere population, thermal desorption seems to play a minor role only causing a smearing at the locations where Na atoms are released on the dayside. The observed and simulated distributions agree very well with this hypothesis and indicate that the combination of the proposed processes is able to explain the observed features.

1 Introduction

In 1974, the UVE experiment on board Mariner 10 (Broadfoot et al., 1976) observed a tiny exosphere around Mercury, made of hydrogen, helium, and, probably, oxygen. Starting from 1985 (Potter and Morgan, 1985), many ground-based observations have identified the presence of sodium in Mercury's exosphere. Most of these observations indicate either north-south or dawn-dusk asymmetries (see Killen et al., 2007, for a recent review on observations). Several processes, such as ion sputtering (IS), thermal desorption (TD), photon-stimulated desorption (PSD), and micro-meteoroid vaporization, have been proposed for being responsible for the formation of the sodium exosphere (e.g., McGrath et al., 1986; Hunten et al., 1988; Potter and Morgan, 1997; Madey et al., 1998; Yakshinskiy and Madey, 1999; Killen et al., 1999, 2001, 2004, 2007; Leblanc and Johnson, 2003; Wurz and Lammer, 2003). In fact, Leblanc and Johnson (2003) concluded in their study that the sodium surface density distribution becomes significantly non-uniform from the day to the night side, and from low to high latitudes as well as from the morning to the afternoon due to the rapid depletion of Na atoms in the surfaces of grains mainly driven by thermal depletion. Killen et al. (2004) suggested that ion precipitation increases the diffusion from the interior.

Recently, Schleicher et al. (2004) published sodium tangential column densities, derived from observation of Mercury transit of May 2003. These column densities show a strong dawn-dusk asymmetry, an enhancement near the poles, and a moderate north-south asymmetry. Also, the reported scale heights are several 100’s of km, which is difficult to reconcile with thermal desorption using realistic temperatures. The aim of the present study is to investigate the possibility that these features may be the result of two combined processes:

1) space weathering of the surface by precipitating solar wind protons, which cause chemical liberation of sodium atoms at the surface, and

2) photon-stimulated desorption of the liberated sodium from the surface into the exosphere.

For this purpose we have developed a numerical model that is able to reproduce the proposed processes and which allows the comparison of the simulated data with the

observations. Already in earlier observations Na and K were sometimes found in localized enhancements at elevated latitudes, which was associated with solar wind entry through the magnetospheric cusps. Also dawn-dusk asymmetries were observed earlier, with pronounced Na and K dawn enhancements. A possible explanation for these features was by recycling of Na and K, which become ionized in the exosphere, enter the magnetospheric system, and with some probability are implanted on the surface again (Sprague, 1992; Hunten and Sprague, 1997). Diffusion will bring these atoms back to the surface where they will thermally desorb. Diffusion of Na and K from locations in the regolith to the surface has been studied in detail (e.g., Sprague 1992; Killen et al., 2004). Since diffusion and desorption are both thermally driven processes, they will not occur on the night side and implanted Na and K will accumulate there until Sun rises. Accumulation of Na and K on the night side explains in a natural way the dawn-dusk asymmetry and the enhancements at high latitudes, the latter because of the regions of ion precipitation on Mercury's surface.

In Section 2 we give a brief outline of the observations; in Section 3 the numerical model used to simulate the data is described. A discussion of the results is given in Section 4, followed by a summary and conclusion in Section 5.

2 Observations

On May 7, 2003, a transit of Mercury across the solar disk occurred. On the occasion of this optimal observation configuration, Schleicher et al. (2004) obtained a series of 2D spectra of the solar sodium resonance line at 589.0 nm (D2), with Mercury being positioned near the field-of-view during the ~2 hours of observation (UT 8:27 to 10:25). At each location h above the limb and at azimuth φ, the column density *along the line of sight* $n(h,\varphi)$ has been derived from the observed equivalent widths $W_\lambda(h,\varphi)$ from the curve-of-growth relation for an absorption tube. For the Doppler-width of the absorption profile the value measured from the observed averaged profile of the excess absorption was used. The equations are given in the appendix section. The derived tangential column densities are displayed in figure 1.

These observations show a maximum Na density at the planetary limb, exponentially decreasing with altitude. The density around the limb, however, is not uniform: two maxima can be found near the polar regions, with a prevalence of the northern one. There, the Na column density along the line of sight (in the following referred as "tangential column density") is up to 8×10^{10} cm^{2}, and the estimated volume density at the surface is 2.6×10^{3} cm^{3} (Schleicher et al., 2004); the presence of sodium is noticeable up to more than 700 km above the surface. Between the two peaks, along the dawn limb, a density excess can be seen. If we integrate the tangential column density over the entire field of view, we obtain a total Na content in the exosphere of 4×10^{27} atoms. From the Doppler width of the line profile of the excess absorption, Schleicher et al. (2004) estimated that the parallel component of the velocity distribution was 1.6 km s^{-1}, which may corresponds to a very high temperature (~3500 K) if we assume a Maxwellian distribution of the particles.

[Figure 1]

3 Model Description

The general concept, underlying our simulations is that the surface abundance of sodium is depleted by thermal and photon-stimulated desorption, and refueled by the solar wind precipitation. In our study, we assume that for each solar wind proton precipitating onto the surface, with some probability a sodium atom will eventually be available at the surface , as the result of chemical alteration of the mineral grain (described below). Hence, we first evaluated the solar wind proton flux onto Mercury's surface corresponding to the solar activity conditions during the transit observations. Then we simulated the sodium surface composition, which was finally used as an input for our 3D exosphere model.

At the time of the considered observations of Mercury exosphere, the planet was 0.45 AU away from the Sun, at an anomaly angle of about 150°. The real physical conditions in the solar wind (in particular speed, density, IMF, etc.) and the solar irradiative

105 background near Mercury during the transit are of critical importance for interpretation of
106 its exosphere observations and verification of the applied models. According to the
107 GOES satellite synoptic data, the Sun was relatively quiet during the whole transit of
108 Mercury on May 7, 2003, with just 3 X-ray events of C-class registered, of which only
109 one in the northern hemisphere (N15E88, C2.2 from 10:17 till 10:27) took place during
110 the performed observations, near the end of the transit. From these data it is justified that
111 we use as an input the average quiet Sun radiation flux in our model.

112 Because of the absence of *in-situ* measurements of the solar wind plasma parameters
113 near Mercury at the time of the transit, we used for their estimation the solar wind data
114 measured by the ACE satellite which is located downstream of Mercury at the Lagrange
115 point L1 at 1.5×10^6 km from the Earth. The fact that Mercury's transit was observed from
116 the Earth, and the ACE spacecraft is also located close to the Sun-Earth line, it makes it
117 possible to assume that the solar wind flow measured by ACE within the next 1 to 2 days
118 after the Mercury transit belongs to the same stream of the solar wind that passed near
119 Mercury.

120 Figure 2 shows the ACE data, measured components of magnetic field, solar wind
121 proton speed and density, as well as the distance from the spacecraft to Earth, during the
122 Mercury transit on May 7, 2003 (day of year 127) and two days after the transit
123 (http://www.srl.caltech.edu/ ACE/ASC/level2/index.html). As it can be seen, a relatively
124 fast interplanetary CME passed ACE with a velocity ~ 890 km s^{-1}) on May 9, 2003.

125

126 [Figure 2]

127

128 However, taking into account the speed of this CME and mutual location of Mercury
129 and the ACE spacecraft, one can calculate that the CME passed Mercury after the transit.
130 Similar treatment of other parts of the solar wind speed curve measured by ACE makes it
131 possible to conclude that the solar wind portion with the speed ~ 780 km s^{-1}, registered by
132 ACE on May 8, 2003, was very likely passing Mercury on May 7, 2003 during the transit
133 observations. Taking into account the decrease of the solar wind speed with distance from

the Sun, we extrapolate ACE values down to the Sun and estimate the solar wind speed near Mercury during the transit on May 7, 2003 as ~ 800 km s^{-1}. Using ACE magnetic field measurements (see Figure 2) and taking into account the decrease of magnetic field with distance (~ $1/r^2$), as well as solar wind motion, the components of the IMF at Mercury during the transit on May 7, 2003 can be estimated as (-20, 10, -10) nT.

The proton precipitation flux, which is needed for the exosphere modeling, was obtained by using a single- particle model (Delcourt et al., 2003, Mura et al., 2005). The original magnetic field model (Luhmann and Friesen 1979, Delcourt et al., 2003) was adapted to the specific conditions at Mercury by adding the IMF field. The resulting proton flux onto the surface has the general shape similar to that presented in Mura et al. (2005). The total flux in the northern hemisphere is about 4×10^{25} s^{-1}, while the negative IMF *x*-component introduces a flux enhancement in the southern hemisphere similar to the results in Sarantos et al. (2001).

3.1 Chemical alteration of the surface composition

The impact of energetic ions (solar wind or magnetospheric ions) on the surface affects the topmost layer of the regolith. The induced processes are ion implantation, sputtering of surface material, and chemical alteration, where the latter allows the breaking of existing and creation of new chemical compounds. Production of sodium and water by proton sputtering of sodium-bearing silicates was considered by the following mechanism (Potter, 1995)

$$2H + Na_2SiO_3 \rightarrow 2Na + SiO_2 + H_2O: \quad (1)$$

The free energy of this reaction is -4.7 kcal/mole, therefore it will proceed spontaneously; however, the activation energy is unknown. Together with the liberated Na, water is produced, with the supply rate of water molecules being half the supply rate of Na by this process. The solar wind protons are implanted into the regolith grains and are neutralized there. The proton fluxes onto the surface are high and saturation of the regolith grains with hydrogen can be safely assumed, which assures the availability of hydrogen for the chemical reaction given above. In summary, hydrogen reacts with the

sodium bearing rock, the Na atoms are liberated from their chemical bounds in the crystal. Since the ion implantation is close to the surface, the atomic Na is produced near the surface and will diffuse thermally to the surface. Atomic Na at the surface can be easily released into the exosphere either by TD or by PSD (Yakshinskiy and Madey, 1999; 2004; Yakshinskiy et al., 2000). The process described in equation 1 causes also the production of water. The global source rate fot H_2O should be roughly half of that of Na, even if the total exosphere content can be different because of different lifetimes. It is worth noting that, recently, FIPS instrument on board MESSENGER has discovered water group ions (Zurbuchen et al., 2008).

3.2 Surface composition model

The planetary surface was divided into 24×48 (latitude, longitude) surface elements. Each surface element had a variable value for the sodium relative composition, $C(t)$, which gives the numerical fraction of free sodium in the elementary surface with respect to the total surface density. The time resolution of the simulation was 10 minutes; the simulation lasted for a full Mercury's day (176 days). For each surface element, we calculated the temporal evolution of $C(t)$, taking into account:

i) the planetary rotation and orbit;

ii) the solar wind proton precipitation;

iii) the photon-stimulated desorption;

iv) the thermal desorption;

v) the photoionization of sodium.

At each step, we first calculated the position of each surface element with respect to the Sun, taking into account the planetary rotation and orbital speed. The apparent angular velocity of the Sun is assumed constant. In fact, we were far from the perihelion where the apparent angular velocity has large variability (where it is retrograde for few days).

Then, for each surface element we calculated the photon-stimulated desorption rate:

$$\Phi_{PSD}(t) = N\ C(t)\ \Phi_{\gamma}\ \sigma\cos(\alpha) = A\ C(t), \quad (2)$$

where Φ_{PSD} is the PSD neutral flux, Φ_{γ} is the relevant photon flux (3×10^{15} cm^{-2} s^{-1} at 1 AU; the flux is scaled as $1/r^2$), σ is the PSD cross-section (2×10^{-20} cm^2, Yakshinskiy and Madey, 1999), N is the surface density (7.5×10^{14} cm^{-2}, Killen *et al.*, 2001), α is the instantaneous angle from the sub-solar point (for $\alpha > 90°$, Φ_{psd} is obviously zero).

To calculate the value of C at the equilibrium, we set $C(0) = 0$ and calculate the value of $C(t)$ at the next integration step, by solving the following differential equation:

$$N\frac{dC(t)}{dt} = k\,\Phi_{PREC} - \Phi_{PSD}(t) = k\,\Phi_{PREC} - A\,C(t), \quad (3)$$

where A is defined in Eq. 2; Φ_{PREC} is the flux of precipitating protons, and k is the product of the overall process yield and the probability for the proton to interact with a Na atom in the surface; by considering the fraction of Na bearing minerals (Feldspars) in the regolith (Wurz *et al.*, 2008), here we have assumed that k is about 5%.

When a surface element is on the dayside, $C(t)$ raises or decreases exponentially, until it reaches the equilibrium:

$$\Phi_{PSD} = k\,\Phi_{PREC}; \quad (4)$$

the time-scale for the equilibrium is:

$$T_{SC} = (\Phi_{\gamma}\sigma)^{-1} \quad (5)$$

which is of the order of one hour. When a surface element is on the night side, $C(t)$ increases if $\Phi_{prec} > 0$ (i.e., magnetospheric protons precipitate onto the surface) until this surface element reaches the dawn terminator. Then, $C(t)$ is rapidly decreased by PSD following Eq. 3. This leads to a maximum of concentration close to the dawn terminator, and hence to a dawn-dusk asymmetry of C.

Note that the total amount of sputtered sodium particles has to be proportional (see Eq. 4) to the total flux of proton precipitating onto the surface. Hence, the parameters Φ_{γ}, and σ influence only on time scales of the simulated density, but they have very small impact on the results at the equilibrium.

Concerning thermal desorption, we find that particles released by TD always fall down onto the surface because their velocities are much lower than the escape velocity. Hence, TD does not contribute to the net flux from the surface. However, as outlined below, the Na atoms fall back within an area of radius <300 km (about 100 km on average, in our simulation). Thus, thermal desorption will cause a smearing of the places of Na release on the dayside. To include this effect in our simulation, we first estimated the TD rate:

$$\Phi_{TD}(t) = \nu \, N \, C(t) \, e^{-\frac{U_{TD}}{k_B T}}, \quad (6)$$

where Φ_{TD} is the neutral flux, ν is the vibration frequency of the adsorbed atoms (10^{13} s^{-1}, Hunten et al., 1988), N is again the regolith surface density, and U_{TD} is the binding energy. This last parameter has a big influence on the desorption rate, and has to be evaluated carefully (Yakshinskiy et al., 2000). Yakshinskiy et al. (2000) determined an energy range for U_{TD} between 1.4 to 2.7 eV. In this study, however, we used an average value for U_{TD} = 1.85 eV, like Leblanc and Johnson (2003). The local temperature of the surface was assumed to vary according to (Leblanc and Johnson, 2003; Wurz and Lammer, 2003):

$$T(\alpha) = T_n + (T_d - T_n)\left[\cos(\alpha)\right]^{1/4} \quad (7)$$

where the sub-solar point temperature (T_d) is scaled between 590 K and 725 K (Vilas, 1988) according to the planetary distance from the Sun. The night side temperature was always 110 K.

Then, for each surface element, we distributed the flux Φ_{TD} to a large number of test-particles. We simulated their ballistic trajectories, starting with a Maxwell-Boltzmann surface velocity distribution with the proper surface temperature. We then evaluated the precipitation position and the lifetime of each test particle, and we redistributed the flux Φ_{TD} accordingly (decreased by photoionization, with lifetime 10^4 s). This latter flux can be considered as an additional source in Eq. 3, while Φ_{TD} can be added to Φ_{PSD} in the sink section of Eq. 3. Hence (as far as photoionization is negligible), the net effect is just a time and spatial blurring of the solution of Eq. 3.

Our simulation lasted one complete Mercury day. However, if we take C in a reference frame fixed with respect to the Sun (i.e., MLT, Mercury Local Time), then C reaches a stable equilibrium after about half a rotation or less (i.e. tens of days). In Figure 3 we show intermediate steps of the temporal evolution of parameter C at different times. After one hour, the dayside configuration is more or less stable. In Figure 4a we show the values of Φ_{PSD} at the equilibrium, in a MLT *vs.* latitude map, and, for comparison, the proton precipitation flux (panel b). Since the flux in the dayside is basically proportional to the proton flux (Eq. 4), the two panels are similar in that area. The dawn-dusk asymmetry of the composition is responsible of the enhancement of Φ_{PSD} close to the dawn terminator (~6:00 MLT).

[Figures 3, 4]

3.3 Exosphere model

To simulate the Na tangential column density in the exosphere of Mercury, we used a Monte-Carlo model. The energy distribution of the emitted Na atoms was extrapolated (Johnson *et al.*, 2002) by laboratory measurements of electron-stimulated desorption (ESD) of adsorbed Na from amorphous ice. It was assumed that the electron energy has little impact on the emitted neutral energy, and that PSD and ESD cause desorption of atoms via similar electronic processes. Johnson *et al.* (2002) have found a good analytical description of the energy spectrum using the following function:

$$f(E) = \beta(1+\beta)\frac{EU^{\beta}}{(E+U)^{2+\beta}}, \quad (8)$$

where β is the shape parameter (0.7 for Na) and U is the characteristic energy, which is of the order of 0.05 eV, for Na. Since the maximum ejection energy should be lower than the photon energy, we used a cut-off function (at about 10 eV) to eliminate the high-energy tail of the function, which we consider unphysical. To evaluate the effect of the source distribution function on the simulated exospheric density, we have also used a different source function:

$$f(E)=\frac{\mathrm{E}}{(k_B T)^2} e^{(-E/k_B T)} \quad (9),$$

since other authors (Yakshinskiy and Madey, 1999, Leblanc and Johnson, 2003) suggested that the energy spectrum has a Maxwellian Boltzmann flux distribution, with T of the order of 1000 to 1500 K.

A large number (>10^6) of test particle trajectories were simulated; a weight w was associated to each test particle to reproduce the flux in Eq. 2 (see details in Mura *et al.*, 2007). The trajectories were calculated using the classical equations of motion, including gravity and radiation pressure acceleration. The radiation pressure acceleration, for Na, can be up to 54% of the surface gravity, ranging between 20 and 200 cm s^{-2}, being function of the photon flux and of the amount of Doppler shift out of the Fraunhofer features (Smyth and Marconi, 1995; Potter *et al.*, 2002). Here we calculate this acceleration as in Leblanc and Johnson, (2003), i.e. we calculate the Doppler shift as a function of each particle's velocity, and then we calculate the acceleration; on average, at 0.45 AU, this is 60 cm/s^2, in the anti-sunward direction.

We defined a 3D cubic accumulation grid extending between -12 $R_M \leq x \leq 3$ R_M (30 steps) and -2 $R_M \leq y, z \leq 2$ R_M (60 steps), with R_M=2439 km being the radius of Mercury and x pointing towards the Sun, z pointing towards north pole (MSE reference frame). The grid has wider x boundaries to enclose all the Sodium (see, for example, Potter *et al.*, 2002). The Na density inside one grid cell was calculated taking into account the number of test particles, the weight w and the lifetime inside the cell. Finally, we integrated the simulated Na density along the x direction to obtain the tangential column density, to be compared directly with the observations.

4 Results and discussion

4.1 Model results

To reproduce the observed tangential column density, we need to assume some values for the simulation parameters. As already mentioned, TD causes just a temporal and spatial smearing of the signal, so the related physical parameters have a small impact on

300 the simulations. Leblanc and Johnson (2003) arrived at the same conclusion when they
301 compared the residence time of sodium atoms related to TD, PSD and sputtering in
302 Mercury's upper surface versus the solar zenith angle. It was found that TD is the most
303 efficient desorption process at low zenith angles but at higher zenith angles PSD and
304 sputtering become more efficient.

305 One of the most important parameters to be considered is the energy U (in Eq. 8),
306 which controls the energy distribution of the emitted sodium atoms. A best fit between
307 data and simulations to find the optimum value for U is not easy; however, we found that
308 a good agreement between observations and simulation can be obtained by taking U =
309 0.086 eV. In Figure 5a the result of the simulated sodium tangential column density is
310 given. As it can be seen, the simulated data show the same features as the observed ones
311 (Figure 1), which are the dawn-dusk and the north-south asymmetry. In the simulation we
312 find that the maximum tangential column density is located at the limb in the north-dawn
313 region and has a value of about 6×10^{10} cm^{-2}.

314

315 [Figure 5]

316

317 Moreover, the apparent scale-height is similar to that in the observations (Figure 1).
318 This parameter results from the chosen energy distribution for the release of the particles:
319 a more energetic source distribution produces higher scale-heights. To evaluate how
320 sensitive our model is to the chosen energy distribution, we produced a similar
321 simulation, using Eq. 9 instead of Eq. 8, with T=1000 K. This energy distribution is
322 somewhat less energetic than the previous one (Mura *et al.,* 2007); the result of the
323 simulation is shown in Figure 5b. There is a substantial resemblance between the two
324 simulations, and it is difficult to tell just by visual inspection which fits better with the
325 observations However, apparently the scale height of the first energy distribution (Eq. 8)
326 fits better with the observations.

327 More information on the energy distribution of the source can be obtained from the
328 observed velocity distribution. To study the velocity distribution of Na in the x direction,

a fourth dimension of the accumulation grid, consisting of 100 velocity steps from -10 to +10 km/s, was included. In this way we were able to estimate the velocity distribution shown in Figure 6. According to Schleicher et al. (2004), the observed velocity distribution can be reproduced by a Gaussian function with a width v_{th} = 1.6 km/s. As shown in Figure 6, the simulation is able to reproduce this feature reasonably well using the energy distribution of Eq. 8. The small secondary peak, visible at about 2 km/s in the figure, is probably due to the radiation pressure acceleration, which originates in the tail up to few R_M behind the planet. In fact, this is the value that can be obtained by simple calculations assuming an acceleration of -60 cm/s^2 and a tail size of about 3 R_M as reported by Potter et al. (2002). For comparison, the velocity distribution obtained using Eq. 9 (dashed line in Figure 6) substantially differs from the previous two. We concluded that the source energy distribution is likely to be more energetic than a Gaussian at 1000 K.

The effect of the radiation pressure acceleration on the observed column densities is negligible; in fact, since this force acts parallel to the line of sight, the first order effect is null. To evaluate the effect of the radiation pressure, we removed this force from the model: the simulated tangential column densities were very similar, almost identical, to those shown in Figure 5a; however, the fraction of escaping Na particles dropped down by a factor 2. We concluded that the radiation pressure acceleration, in the present configuration, is responsible of about 50% of the Na escape rate.

[Figure 6]

Table 1 gives a summary of the observed and simulated physical quantities. The tangential column densities are very close. However, the typical scale height in the model calculations is higher than in the observations and therefore the total amount of Na in the simulation is higher than that in the observations.

[Table 1]

The gardening rate at Mercury is estimated to cause a grain lifetime on the surface of the order of 10^4 - 10^5 years (Horz *et al.*, 1991); a complete discussion about how this lifetime implies diffusion-limited supply rates in the exosphere of Mercury can be found in Killen *et al.* (2004). These authors found that a supply rate up to 10^7 cm^{-2} s^{-1} is

359 consistent with a diffusion limited supply of Na. For comparison, in our study, the
360 average PSD flux on the surface was found to be of the order of 10^7 cm^{-2} s^{-1}, but the local
361 PSD rate (see Figure 4) was higher in the areas of intense proton precipitation. This is
362 consistent with the results of Killen *et al*., (2004) when saying that higher supply rates
363 can be the result of ion-enhanced diffusion.

364

365 **4.2 Ion sputtering**

366 The presence of the two maxima observed at high latitude is a hint for the presence of
367 a space weathering process, such as ion sputtering. Hence, we simulated the Na
368 exospheric density resulting from this process. We assumed that the proton precipitation
369 flux was the same as shown in Figure 4b. Each impinging proton has some probability
370 (yield, *Y*) to extract a neutral sodium atom from the surface; this probability is related to
371 the proton energy (Lammer *et al.*, 2003); we have assumed an averaged value of 10% for
372 simplicity. Other solar wind components, like α particles or high-charge-state particles,
373 produce a comparable amount of ion sputtering (Johnson and Baragiola, 1991).
374 Assuming that their precipitation patterns are similar to that of protons, we assumed a
375 weighted yield of 20% as an upper limit for sputtering. The resulting Na flux is hence:

376 $$\Phi_{IS} = Y\, c\, \Phi_{PREC} \quad (10)$$

377 where *c* is the surface abundance of sodium in the surface. While thermal and photon-
378 stimulated desorption act on the extreme surface (a few monolayers, where the
379 concentration of Na should be calculated as in Section 3.2), ion-sputtering extracts
380 sodium from deeper and in a stoichiometric way. Hence, we assumed *c* uniform all over
381 the surface and equal to 0.5% (Goettel, 1988).

382 The energy distribution of the ejecta can be simulated using the following function
383 (Siegmund, 1961; Betz and Wien, 1994):

384 $$f_S(E_e) \propto \frac{E_e}{(E_e + E_b)^3}\left[1 - \left(\frac{E_e + E_b}{E_i}\frac{(m_H + m_{Na})^2}{4\, m_H m_{Na}}\right)^{\frac{1}{2}}\right], \quad (11)$$

where E_e is the ejection energy, E_i is the proton energy, E_b is the binding energy (here 2 eV, as in Lammer *et al.,* 2003). We used this as an input for the exospheric model, then we integrated the result to obtain the tangential column densities to be compared with the observations. The result is shown in Figure 7a. There are at least three discrepancies between this simulation and the observations:

- the tangential column densities are about two orders of magnitude lower than those observed; in fact, for each proton, only 0.05% of Na is sputtered, i.e. released into the exosphere (Y times c).
- the simulated scale-heights are considerably larger than those observed; in fact the energy distribution in Eq. (11) is more energetic than that in Eq. (8);
- there is no evident dawn-dusk asymmetry.

In summary, ion sputtering, alone, is not able to explain the observed features. Moreover, since the contribution to the total column densities is only about 1% of the observed values, which is consistent with the results from Wurz *et al.* (2007), it is possible to neglect its contribution in the particular configuration of the present study. On the other hand, since the process is more energetic, most of sputtered Na are either photoionized (due to longer ballistic time) or lost (due to Jeans escape). Hence, this process must be taken into account while simulating the Na tail, as in section 4.4.

4.3 Meteoritic and micrometeoritic impact vaporization

Mercury is exposed to the constant precipitation of particles of small sizes (<100 μm), impacting the surface at a mean velocity of 20 km/s (Cintala, 1992), churning the regolith and vaporizing the surface. Larger objects impact the surface as well, causing local enhancement of the sodium exospheric density (Mangano *et al.*, 2007), but the contribution by these meteorites to the global Hermean exosphere is considered to be negligible (Killen *et al.*, 2007). Morgan et al. (1988) reported an average value of 2×10^5 (cm^{-2} s^{-1}) released Na at aphelion, a factor 2 higher than the value reported by Cintala (1992) (see Killen *et al.*, 2007 for a detailed discussion). The first value, which we have used here as a worst case, is a factor 100 lower than our averaged PSD flux. If we assume that the ejecta have a thermal velocity distribution at about 2500 K (Killen et al., 2007),

and that the precipitating particles are uniformly distributed over the surface, we obtain the simulated Na tangential column densities of Figure 7b. Obviously, the precipitation flux could be not uniform on the surface and so our estimation of the density due to impact vaporization is probably locally inaccurate to a factor of two (Killen et al., 2004); however, this simulation shows that, at a first order of approximation, we can discard impact vaporization as a main Na source in this particular observing configuration.

4.4 The sodium tail

The presence of a sodium tail, extending in the anti-sunward direction, has been first observed by Potter *et al.* (2002). Since this is an important feature of the sodium exosphere, it should be taken into account by any model. In this section we discuss the formation of the Na tail within our present model. The sodium tail is formed by those Na atom whose ejection energy is higher than the gravitational escape energy (2.07 eV), or by that atoms that can overcome the gravitational field thanks to a partial contribution of the radiation pressure acceleration. These particles are accelerated by the radiation pressure in the anti-sunward direction. In addition, photoionized Na can be picked-up by the solar wind. The radiation pressure acceleration during the observation time, at 150° anomaly angle, was about 60 cm s^{-2}, well below the maximum (200 cm s^{-1}), which occurs at about 60° and 300° anomaly angle (Smyth and Marconi, 1995; Potter *et al.,* 2002). The relation between the solar radiation pressure and the tail formation has been recently investigated by Potter and Killen (2008). According to these authors, the tail is not detectable from Earth with a radiation pressure below about 100 cm s^{-2}. In our case, the acceleration was lower (60 cm s^{-2}), but the proton precipitation was very intense, due to the extreme solar wind conditions (see section 3). Hence, in our case we should obtain a very faint tail. To simulate it, we used all the four processes described previously as a source for our exospheric model; the PSD source function is that given in Eq. 8. The result is shown in Figure 8. Such a tail is very faint and probably hard to observe from Earth; in fact, in the nightside, the densities are 2 to 4 orders of magnitude lower than those in the dayside. The contribution of thermal desorption is negligible, since only 3% of the desorbed particles do not re-impact onto the surface, and only due to photoionization. Also impact vaporization does not contribute significantly, since only 10% of the ejected particles are able to escape, mostly due to photoionization. The

fraction of particles desorbed due to photon-stimulation that escape was found to be between 1% and 10%, depending on the source function we used, while 50% of the ion-sputtered particles are able to escape. However, since surface flux for PSD is higher, both these two processes contribute significantly to the formation of the sodium tail. A summary of these values can be found in table 2. We conclude that, in general, our model is consistent with the existence of a sodium tail.

[Table 2]

Recently, the sodium tail has been observed during the first MESSENGER flyby (McClintock *et al.,* 2008). These authors have found that, at 2 R_M down the tail, the traverse column density was ~3.4×10^9 atoms cm^{-2}. In our simulation, we found, for the same quantity, a value slightly less than 10^9 cm^{-2}. Even if a detailed comparison is beyond the scope of this study, we note that there is no contradiction between these values. In fact, during those MESSENGER observations, the radiation pressure was close to its maximum, i.e. three times higher than that assumed in this study.

5 Model limitations

A critical hypothesis in our model is to assume that the proton precipitation flux (on the night side) is constant over a very long time-scale (~ weeks), which is clearly a major simplification. However, as discussed in Section 3.2, the time-scale for the equilibrium between proton fluxes and PSD fluxes is very short on the dayside (about one hour). Therefore, we propose the following explanation. The north-south asymmetry is due to the proton precipitation on the dayside, which rapidly results in an enhancement of the Na density in the high latitude regions (by means of the combined mechanism described in Section 3.1). The dawn-dusk asymmetry, on the other hand, is caused by the planetary rotation, which is always in the same direction (except a few days of apparent retrograde Sun motion), and by the presence of some magnetospheric proton precipitation on the night side; such a precipitation is predicted for most of the IMF conditions (see, for example, Kallio et al., 2003, or Mura et al., 2005). Hence, in this first study we did not perform a detailed estimation of the proton circulation and precipitation; moreover, the TD effect causes a smearing of the surface composition, so that a detailed map of the proton precipitation is not needed.

475

476 **6 Summary and Conclusions**

477 We presented a model for the formation of Mercury's sodium exosphere as it was
478 observed during the Mercury transit on May 7, 2003, involving two steps for the release
479 of Na atoms from the surface. The first step is the liberation of Na from the chemical
480 environment of the mineral by implantation of energetic hydrogen and subsequent
481 chemical reaction. The second step is photon-stimulated desorption of Na into the
482 exosphere. Thermal desorption only smears the location where the Na atoms are released.
483 For the simulation of this two-step process, a 3D exospheric model was adapted
484 accordingly.

485 Comparison of our model results with measurements by Schleicher et al. (2004) show
486 good qualitative agreement in the structure of Mercury's sodium exosphere. Our model
487 reproduces the high latitude features, and the asymmetries in the north-south and in the
488 dawn-dusk direction. Concerning the quantitative comparison, the simulated Na total
489 amount is of the same order of magnitude as that derived from observation. There are,
490 however, at least 3 parameters that control this value:

491 1) *The scale height*. The parameter U in Eq. 8 controls the energy distribution of the
492 PDS emitted Na, and hence the scale-height of the simulated exosphere. A larger scale-
493 height in the model causes the dayside population (which is the most relevant one) in the
494 simulations to rise above the planetary limb and therefore to become more visible from
495 the night side. Hence, the value of U is also related to the overall Na amount. Since the
496 scale-height of the simulation is higher than that of the observation, this may suggest that
497 a lower value for U should be used. We have also performed some simulations, using a
498 simple Gaussian distribution function (with temperature of 1000 K), instead of Eq. 8.
499 Even if the simulated densities (Figure 5b) and scale-heights were very similar to the
500 observed ones, such energy distribution failed to explain the measured velocity spread.

501 2) *The proton flux*. The simulated densities are proportional to the total precipitation
502 rate, and the shape depends on that of the proton flux onto the surface. In particular, the
503 proton precipitation onto the nightside, thanks to the rotation of the planet, is responsible
504 for the formation of the dawn dusk asymmetry. In addition to proton precipitation other

505 magnetospheric ions will precipitate as well. For example, Na^+ precipitation occur
506 nightside (see Delcourt *et al.*, 2003), which will increase the surface weathering effects.
507 In fact, according to Potter (1995), in the case of chemical sputtering caused by Na^+, the
508 yield should be higher. In any case, the inclusion of any other precipitation or
509 replenishing process occurring on the nightside, which we have neglected in this first
510 simulation, will cause an enhancement of the simulated dawn-dusk asymmetry, and, in
511 fact, the dawn-dusk asymmetry is a somewhat more evident in the observations than in
512 the model. The effect of other ion precipitation on the nightside, as well as impact
513 vaporization, not included in the present simulation, can be estimated using the model. In
514 fact, adding an hypothetical, uniform value of Sodium 2×10^6 cm^{-2} s^{-1} lead to a tangential
515 column density of 4×10^{10} cm^{-2}, which is what is observed close to the dawn terminator.
516 In this way, it is possible to estimate the upper limit of the Na replenishment process that
517 can occur in the nightside as 2×10^6 cm^{-2} s^{-1}.

518 3) *The process yield*. Here, we have assumed that the averaged process yield is 5%,
519 and the simulated densities scale linearly with this parameter. Recently, Sarantos *et al.,*
520 (2008) have studied the influence of ion-enhanced PSD at the Moon, following the
521 mechanism proposed by Potter (2000); the mechanism is somewhat different from that
522 proposed here, but the global result is the same. These authors observed that the ion flux
523 increased to 3×10^7 cm^{-2} s^{-1} during the passage of the Moon in the Earth's magnetotail,
524 and as a result, the PSD rate was higher then expected, and of the order of 2×10^5 cm^{-2} s^{-1}.
525 This would result in an averaged yield of the order of 1%, which is in good agreement
526 with our assumption, also because one could expect that the yield of the process may
527 depend on the ion energy ranges, that may differ from the Moon to Mercury.

528 Since the PSD release Na flux is proportional to the proton precipitation, one could
529 expect that, on the dayside (which is not visible in the observation) the Na exospheric
530 densities should resemble the proton flux in Figure 4b. As shown in Figure 8, however,
531 this is not the case. In fact, on the dayside also the Na population from thermal desorption
532 is present. Moreover, in the case of a non-uniform surface source, Mura *et al.,* (2007)
533 have estimated that the characteristic horizontal scale lengths of the exosphere are about a
534 factor 2 longer than that of the source, due to the ballistic trajectories of the particles.

Another effect, not yet included in this model, can be the Na release due to thermal diffusion, that should be maximal in the sub-solar point region, between our two precipitation maxima (Killen *et al.,* 2004).

The Na density in the tail predicted by our model is also in substantial agreement with that observed during the first MESSENGER flyby (McClintock *et al.,* 2008). Moreover, chemical sputtering of Na by protons causes also the production of water, and it is worth noting that the FIPS instrument on board MESSENGER has discovered such water group ions in the exosphere of Mercury (Zurbuchen et al., 2008).

In a separate simulation run we have tried to simulate the Na density in a different way, by assuming that the proton precipitation causes only direct ion-sputtering of surface sodium. However, the simulated scale-heights were larger and the tangential column densities were about 100 times lower than those observed, because ion-sputtering has a lower yield (5%) and a more energetic velocity distribution. On the other hand, it is difficult to explain North-South asymmetries without including plasma precipitation effects. We also simulated the Na exospheric density arising from impact vaporization; also in this case, the tangential column densities were lower by a factor 100. Presently, it is therefore not possible to explain these observations without including a process that combines ion-precipitation and PSD via the chemical alteration of the surface induced by ion impact.

Appendix

From the detected excess absorption, densities of the sodium atoms in Mercury's exosphere could be derived using the following equations:

$$W_\lambda(h,\varphi) = \int_{-\infty}^{+\infty} \frac{\Delta I_\lambda(h,\varphi)}{I_\lambda} \quad \text{(A1)}$$

$$\frac{\Delta I_\lambda(h,\varphi)}{I_\lambda} = 1 - \exp(-\tau_\lambda) \quad \text{(A2)}$$

$$\tau_\lambda = \kappa_\lambda^{(A)}\, n(h,\varphi) \quad \text{(A3)}$$

$$\kappa_\lambda^{(A)} = \kappa_0^{(A)} \frac{1}{\sqrt{\pi}\Delta\lambda_D} \exp\left(-\frac{\lambda}{\Delta\lambda_D}\right)^2 \quad \text{(A4)}$$

Here, $W_\lambda(h,\varphi)$ is the equivalent width of the absorption excess ΔI_λ, observed at location h above the limb at azimuth φ. I_λ is the solar background intensity (that is the undisturbed solar D_2 line profile). $\kappa_0^{(A)}$ is the atomic absorption coefficient at line center of the resonance line, $\Delta\lambda_D$ the Doppler width of the excess absorption. By inserting Eq. A2-A4 into Eq. A1 one gets the relation between equivalent width and n, the column density *along the line of sight*, which is nearly linear, because the excess absorption is nearly optically thin. Using this relation, the *tangential column densities* displayed in Figure 1 have been derived from the observed equivalent widths; for the Doppler width the value measured from the observed averaged profile of the excess absorption were used.

Acknowledgments

This work was supported by the Italian Space Agency (ASI). A. Mura and H. I. M. Lichtenegger also acknowledge support from the EU funded Europlanet project due to its N5 activity. We also thank the ACE SWEPAM instrument team and the ACE science Center for providing ACE data.

578 **References**

579 Betz, G., and K. Wien. Energy and angular distributions of sputtered particles, Int. J. of Mass Spectrometry
580 and ion processes, 140, 1–110, 1994.

581 Broadfoot A.L., D.E. Shemanky, and S. Kumar, Mariner 10: Mercury atmosphere, Geophys. Res. Lett., 3,
582 577, 1976.

583 Cintala, M. J., 1992. Impact-induced thermal effects in the lunar and mercurian regoliths. J. Geophys. Res.
584 97, 947–973.

585 Delcourt, D. C., S. Grimald, F. Leblanc, J.-J. Berthelier, A. Millilo, A. Mura, S. Orsini, and T. E. Moore, A
586 quantitative model of the planetary Na+ contribution to Mercury's magnetosphere, Ann. Geophys.,
587 21, 1723, 2003.

588 Goettel, K.A., Present bounds on the bulk composition of Mercury: implications for planetary formation
589 processes. In: Vilas, F., Chapman, C.R., Matthews, M.S. (Eds.), Mercury. Univ. of Arizona Press,
590 Tucson, pp. 613–621, 1988.

591 Horz, F., Grieve, R., Heiken, G., Spudis, P., Binder, A., Lunar surface processes. In: Heiken, G., Vaniman,
592 D.T., French, B.M. (Eds.), Lunar Sourcebook. Cambridge Univ. Press, Cambridge, pp. 61., 1991

593 Hunten, D.M., and A.L. Sprague, Origin and character of the lunar and mercurian atmospheres, Adv. Space
594 Res. 19, 1551–1560, 1997.

595 Hunten, D.M., T.H. Morgan, and D.E. Shemansky, The Mercury Atmosphere, In: Vilas, F., Chapman,
596 C.R., Matthews, M.S. (Eds.), Mercury. Univ. of Arizona Press, Tucson, pp. 613–621, 1988.

597 Johnson, R.E., and R. Baragiola, Lunar surface: sputtering and secondary ion mass spectrometry. Geophys.
598 Res. Lett., 18, 11, 2169-2172, 1991.

599 Johnson, R.E., Leblanc, F., Yakshinskiy, B.V., Madey, T.E. Energy distributions for desorption of sodium
600 and potassium from ice: the Na/K ratio at Europa. Icarus 156, 136–142, 2002.

601 Kallio, E. and P. Janhunen, Solar wind and magnetospheric ion impact on Mercury’s surface Geophys. Res.
602 Lett., Vol. 30, No. 17, 1877, 2003.

603 Killen, R.M., A. Potter, A. Fitzsimmons, T.H. Morgan, Sodium D2 line profiles: clues to the temperature
604 structure of Mercury's exosphere. Planet. and Space Sci., 47 1449-1458, 1999.

605 Killen, R. M., Potter, A. E., Reiff, P. H., Sarantos, M., Jackson,B. V., Hick, P., and Giles, B. L.: Evidence
606 for space weather at Mercury, J. Geophys. Res., 106, 20 509–20 526, 2001.

607 Killen, R.M., M. Sarantos, A.E. Potter, and P. Reiff, Source rates and ion recycling rates for Na and K in
608 Mercury’s atmosphere, Icarus 171 1–19, 2004.

609 Killen, R., G. Cremonese, H. Lammer, S. Orsini, A. E. Potter, A. L. Sprague, P. Wurz, M. L.
610 Khodachenko, H. I. M. Lichtenegger, A. Milillo and A. Mura, Processes that Promote and Deplete the
611 Exosphere of Mercury, Space Science Reviews , 132, 433-509, 2007.

612 Lammer, H., Wurz, P., Patel, M.R., Killen, R., Kolb, C., Massetti, S., Orsini, S., Milillo, A., The variability
613 of Mercury's exosphere by particle and radiation induced surface release process. Icarus 166, 238–
614 247, 2003.

615 Leblanc F. and Johnson, R.E., Mercury's sodium exosphere, Icarus, 164, 261-281, 2003.

616 Luhmann, J. G. and Friesen, L. M.: A simple model of the magnetosphere, J. Geophys. Res., 84, 4405–
617 4408, 1979.

618 McClintock W. E., E. T. Bradley, R. J. Vervack Jr., R. M. Killen, A. L. Sprague, N. R. Izenberg, S. C.
619 Solomon, Mercury's Exosphere: Observations During MESSENGER's First Mercury Flyby, 92, 321
620 Science, 2008

621 Madey, T.E., Yakshinskiy, B.V., Ageev, V.N., Johnson, R.E., Desorption of alkali atoms and ions from
622 oxide surfaces: relevance to origins of Na and K in atmospheres of Mercury and the Moon. J. Geophys.
623 Res. 103, 5873–5887, 1998.

624 V. Mangano, A. Milillo, A. Mura, S. Orsini, E. DeAngelis, A.M. DiLellis, and P. Wurz, The contribution
625 of impact-generated vapour to the hermean atmosphere, Planet. Space Sci. 55(11), 1541–1556, 2007.

626 McGrath, M.A., Johnson, R.E., and Lanzerotti, L.J., Sputtering of sodium on the planet Mercury, Nature,
627 323, 694–696, 1986.

628 Morgan, T.H., H.A. Zook, A.E. Potter, Impact-driven supply of sodium and potassium in the atmosphere of
629 Mercury. Icarus 74, 156–170,1988.

630 Mura, A., S. Orsini, A. Milillo, D. Delcourt, S. Massetti. Dayside H+ circulation at Mercury and neutral
631 particle emission. 175, 305–319, 2005.

632 Mura, A., A. Milillo, S. Orsini, S. Massetti, Numerical and analytical model of Mercury's exosphere:
633 Dependence on surface and external conditions, Planet. Space Sci., 2007.

634 Potter, A.E., and T.H. Morgan. Discovery of Na in the atmosphere of Mercury, Science 229, 651-653,
635 1985.

636 Potter, A.E., and T.H. Morgan. Evidence for suprathermal sodium on Mercury. Adv. Space Res. 19, 1571–
637 1576. 1997.

638 Potter, A. E., R. M. Killen, and T. H. Morgan, Variation of lunar sodium during passage of the Moon
639 through the Earth's magnetotail, J. Geophys. Res., 105, 15,073– 15,084, 2000.

640 Potter, A., Killen, R.M., Morgan, T.H., The sodium tail of Mercury, Meteor. Planet. Sci. 37 (9), 1165–
641 1172, 2002.

642 Potter, A., and R.M. Killen, Observations of the sodium tail of Mercury, Icarus 194, 1–12, 2008.

643 Sarantos, M., Reiff, P.H., Hill, T.W., Killen, R., Urquhart, A.L., A . . . -interconnected magnetosphere
644 model for Mercury. Planet. Space Sci. 49, 1629–1635, 2001.

645 Sarantos, M., R. M. Killen, A. S. Sharma, and J.A. Slavin. Correlation between Lunar Prospector
646 measurements and the Lunar Exosphere during passage through the Earth's magnetosphere, Geophys.
647 Res. Lett. 35, L04105, 2008.

648 Schleicher, H., G. Wiedemann, H. Wöhl, T. Berkefeld, and D. Soltau, Detection of neutral sodium above
649 Mercury during the transit on 2003 May 7. Astronomy and Astrophysics, 425, 1119–1124, 2004.

650 Sigmund, P., Theory of sputtering. I. Sputtering yield of amorphous and polycrystalline targets. Phys. Rev.
651 184, 383–416, 1969.

652 Smyth, W. H., and M. L. Marconi, Theoretical overview and modeling of the sodium and potassium
653 atmospheres of Mercury. Astrophys. J. 441: 839-864, 1995.

654 Sprague, A.L., Mercury's atmospheric bright spots and potassium variations: A possible cause, Jou.
655 Geophys. Res. 97 18257–18264, 1992.

656 Vilas, F., Surface composition of Mercury from reflectance spectrophotometry. In: Vilas, F., Chapman,
657 C.R., Matthews, M.S. (Eds.), Mercury. Univ. of Arizona Press, Tucson, pp. 59–76, 1988

658 Wurz, P., and H. Lammer, Monte-Carlo Simulation of Mercury's Exosphere, Icarus, 164 (1), 1-13, 2003.

659 Wurz, P., U. Rohner, J. A. Whitby, C. Kolb, H. Lammer, P. Dobnikar, and J. A. Martin-Fernandez (2007),
660 The lunar exosphere: The sputtering contribution, Icarus, 191, 486– 496, 2007.

661 Wurz, P., J. Whitby, U. Rohner, J.A. Martin-Fernandez, H. Lammer, and C. Kolb, "The Sputter
662 Contribution to Mercury's Exopshere", Icarus, in preparation, 2008.

663 Yakshinskiy, B. V. and T. E. Madey, Photon-stimulated desorption as a substantial source of sodium in the
664 lunar atmosphere, Nature 400, 642 – 644, 1999.

665 Yakshinskiy, B.V., Madey, T.E., Ageev, V.N., Thermal desorption of sodium atoms from thin SiO2 films.
666 Surface Rev. Lett. 7, 75–87, 2000.

667 Yakshinskiy, B.V., Madey, T.E., Photon-stimulated desorption of Na from a lunar sample: temperature-
668 dependent effects. Icarus, 168, 53–59, 2004.

669 T. H. Zurbuchen, J. M. Raines, G. Gloeckler, S. M. Krimigis, J.A. Slavin, Patrick L. Koehn, R. M. Killen,
670 A. L. Sprague, R. L. McNutt Jr., S. C. Solomon, MESSENGER Observations of the Composition of
671 Mercury's Ionized Exosphere and Plasma Environment, 90-92, 321, Science, 2008

672

673

Table 1. Summary of observed and simulated physical quantities

Parameter	Observations	Simulation
Tan. col. dens. (max)	7×10^{10} cm^{-2}	$5\cdot\times10^{10}$ cm^{-2}
Total amount	4×10^{27}	5×10^{27}
Scale height	200 to 500 km	~ 1000 km

Table 2. Loss rates

Parameter	Jeans escape (%)	Photoionization (%)
Photon Stimulated Desorption	5%	25%
Thermal Desorption	<1%	3%
Impact Vaporization	2%	10%
Ion Sputtering	45%	45%

Figure captions

Fig. 1: Observed Na tangential column density during the Mercury transit of May 7, 2003. Data are from Schleicher et al. (2004). *y* and *z* axes are orientated according to the MSE frame (see text), i.e., *z* is positive towards north and *y* is positive towards dusk.

Fig. 2: Measured by ACE, during May 7-9, 2003, distance from spacecraft to Earth, components of magnetic field, solar wind proton speed and density (http://www.srl.caltech.edu/ACE/ASC/level2/index.html).

Fig. 3: Simulated temporal evolution of parameter $C(t)$. The pink line is a meridian line, fixed on the surface.

Fig. 4: Panel a: Simulated Sodium flux due to PSD. The flux in the dayside (8:00 to 16:00 MLT) is basically equal to the H^+ flux (see Eq. 4). The flux close to the dawn terminator (6:00) is enhanced because the Na composition in the night side is enriched by the proton precipitation. Panel b: H^+ precipitation flux.

Fig. 5. Panel a:Simulated Na tangential column density. Panel b: idem, but using the source distribution function in Eq. 9.

Fig. 6. Parallel (x) velocity distribution of the simulated particles (dotted line). The observed velocity distribution can be reproduced by a Gaussian function with v_{th} = 1.6 km/s (solid line). The dashed line shows the simulated velocity distribution using Eq. 9. The small secondary peaks visible at about 2 km/s are due to radiation pressure acceleration.

Fig. 7. Panel a: Simulated Na tangential column density, for Ion sputtering. Panel b: idem, but for impact vaporization.

Fig. 8. Simulated Na density in the *xz* plane. Sun is to the right.

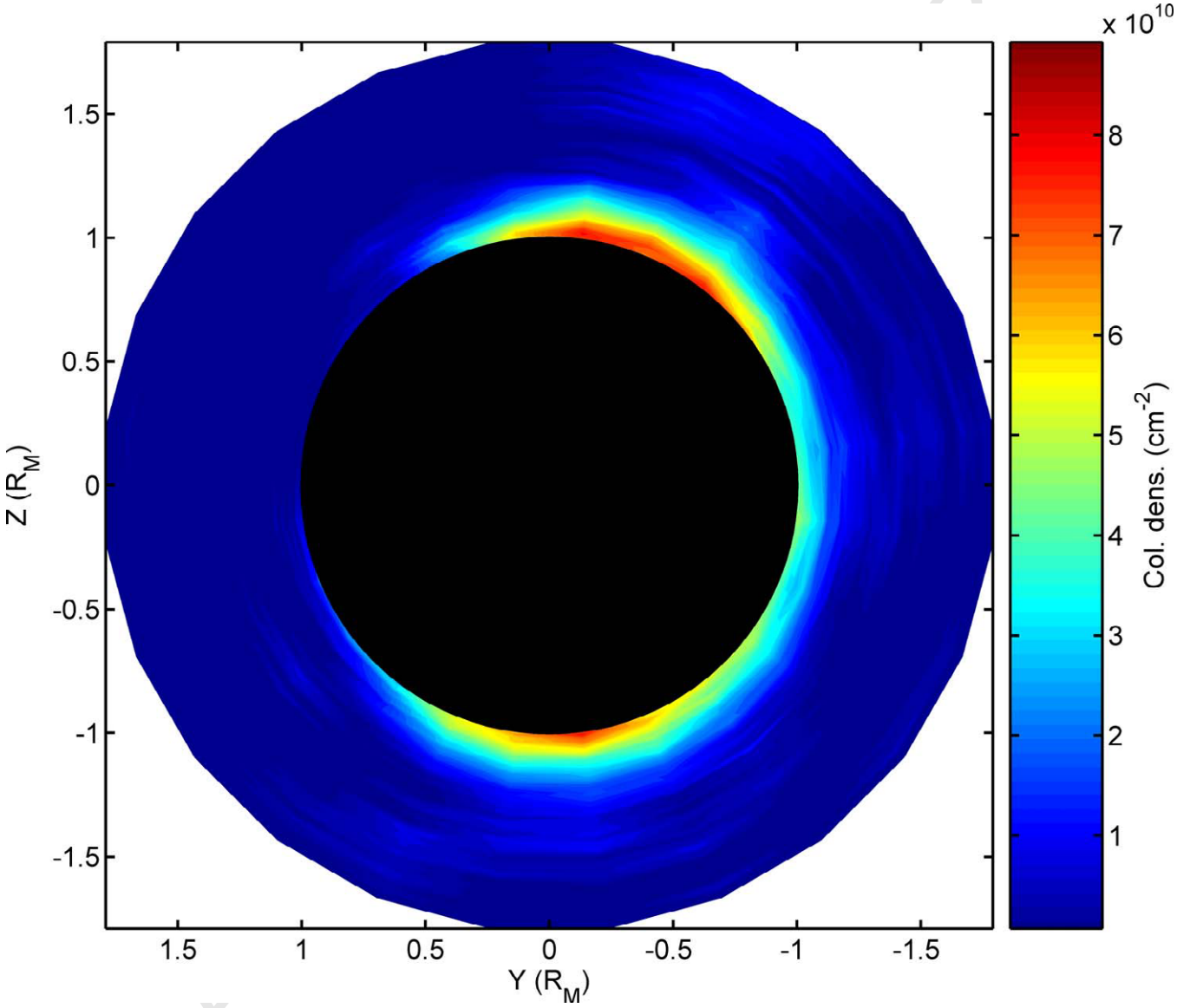

I10475-Fig1

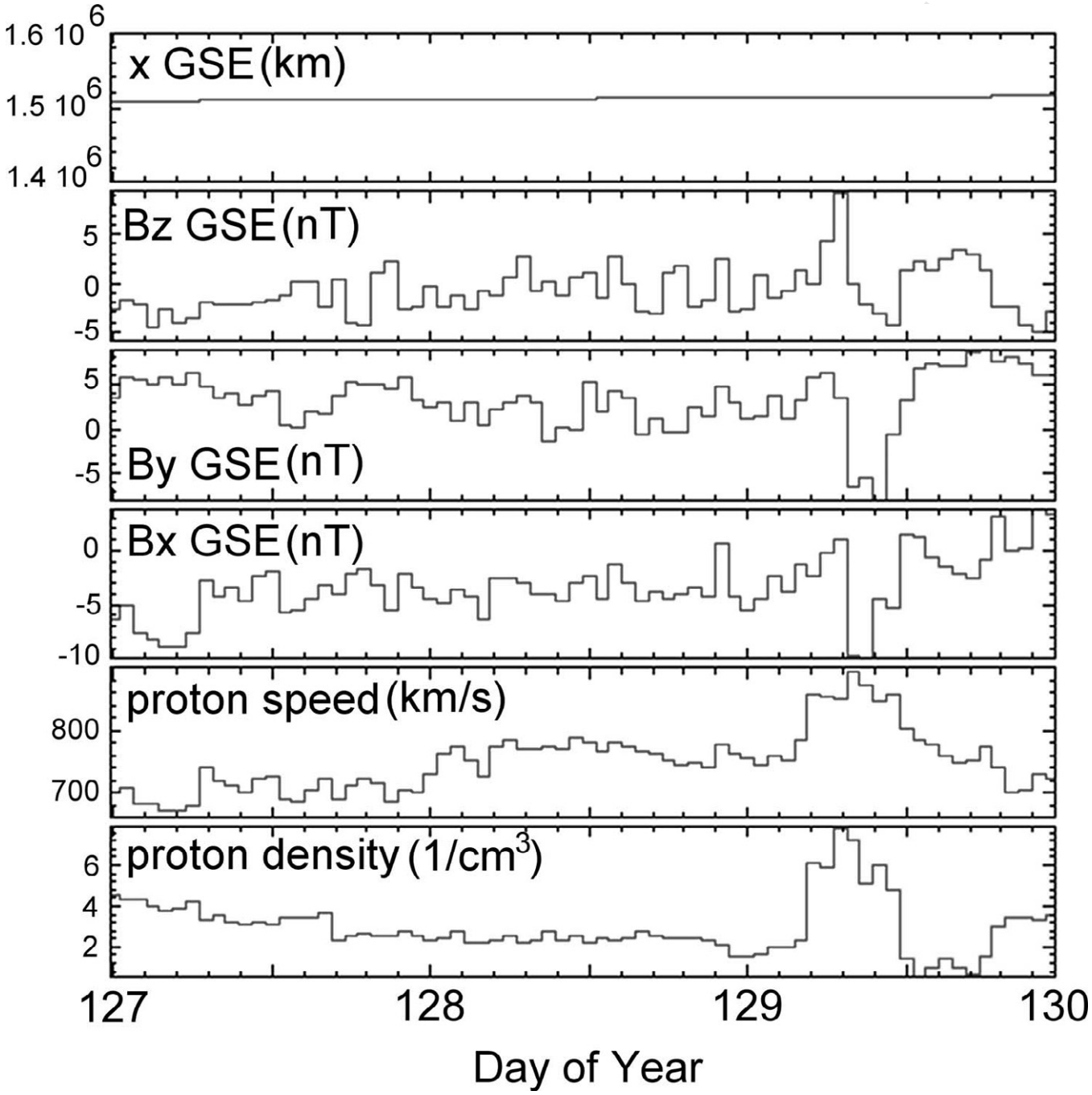

I10475-Fig2

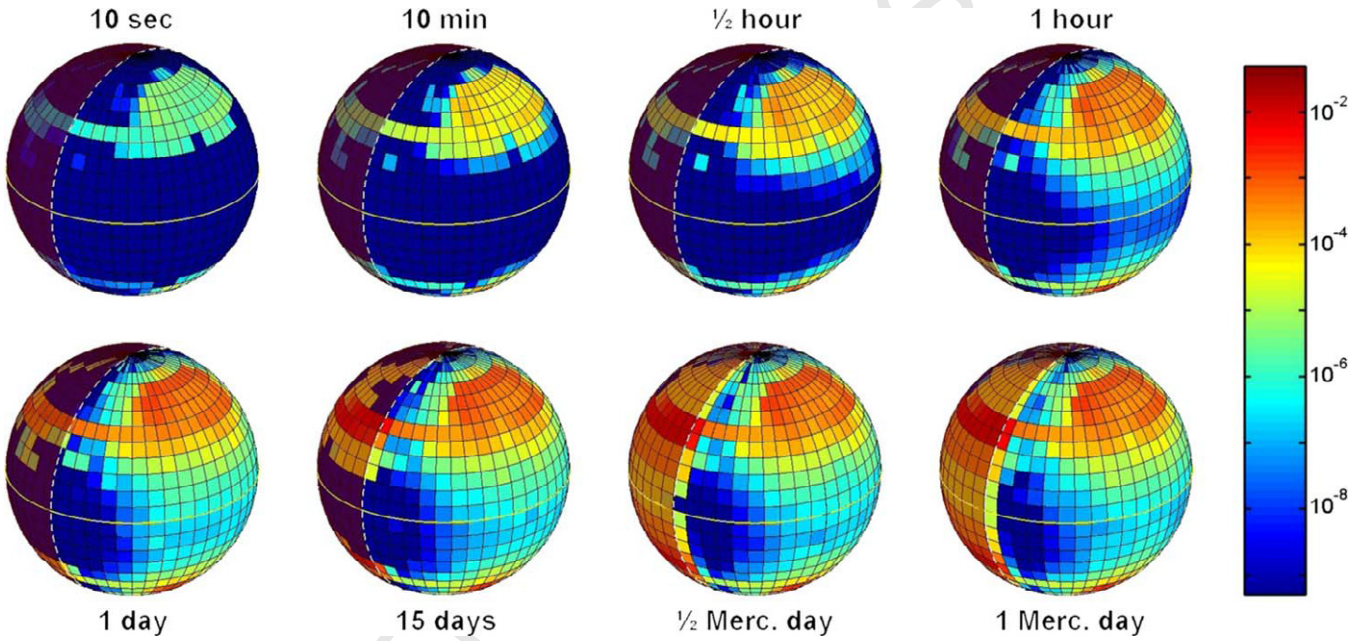

I10475-Fig3

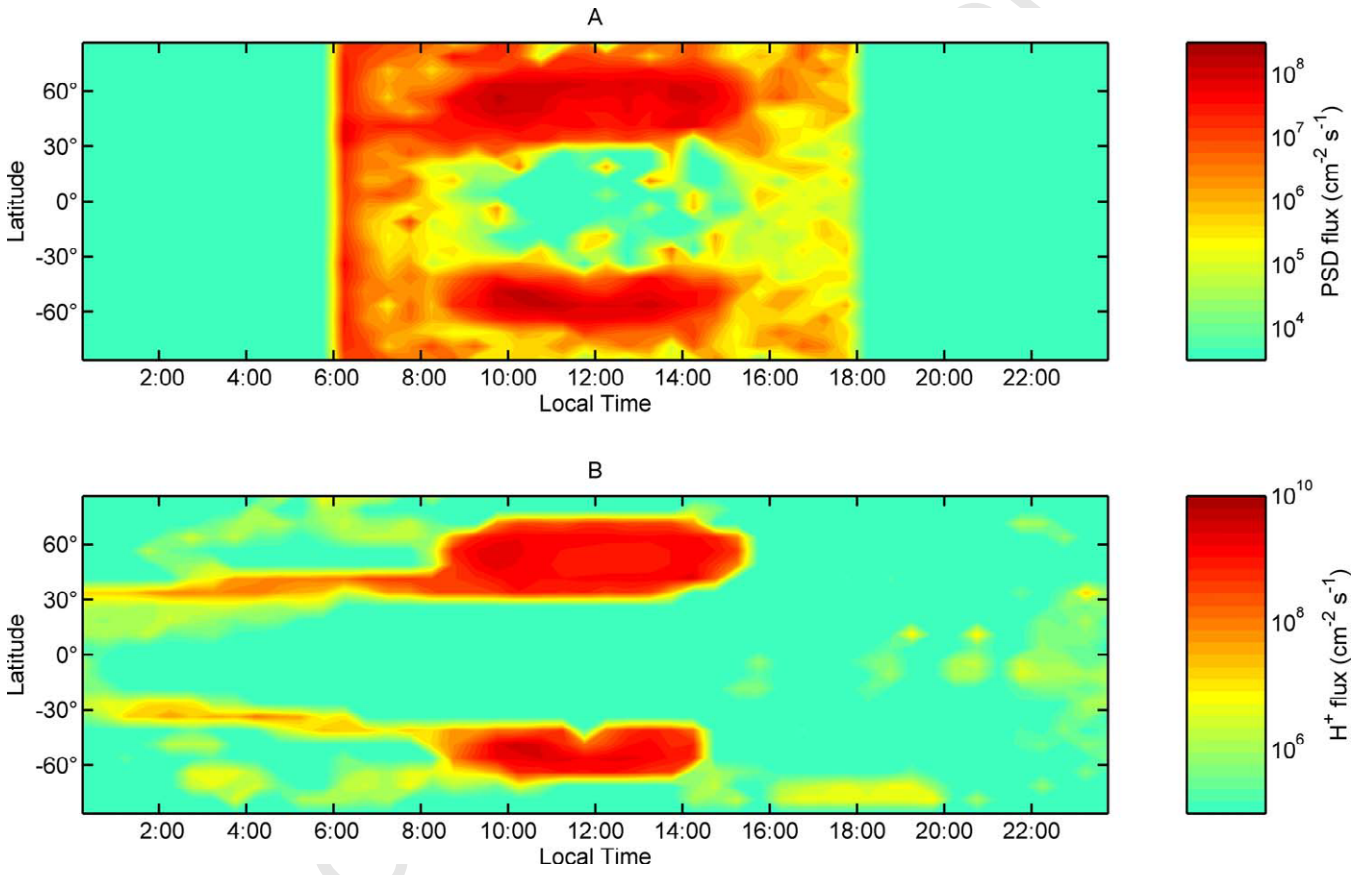

I10475-Fig4-color

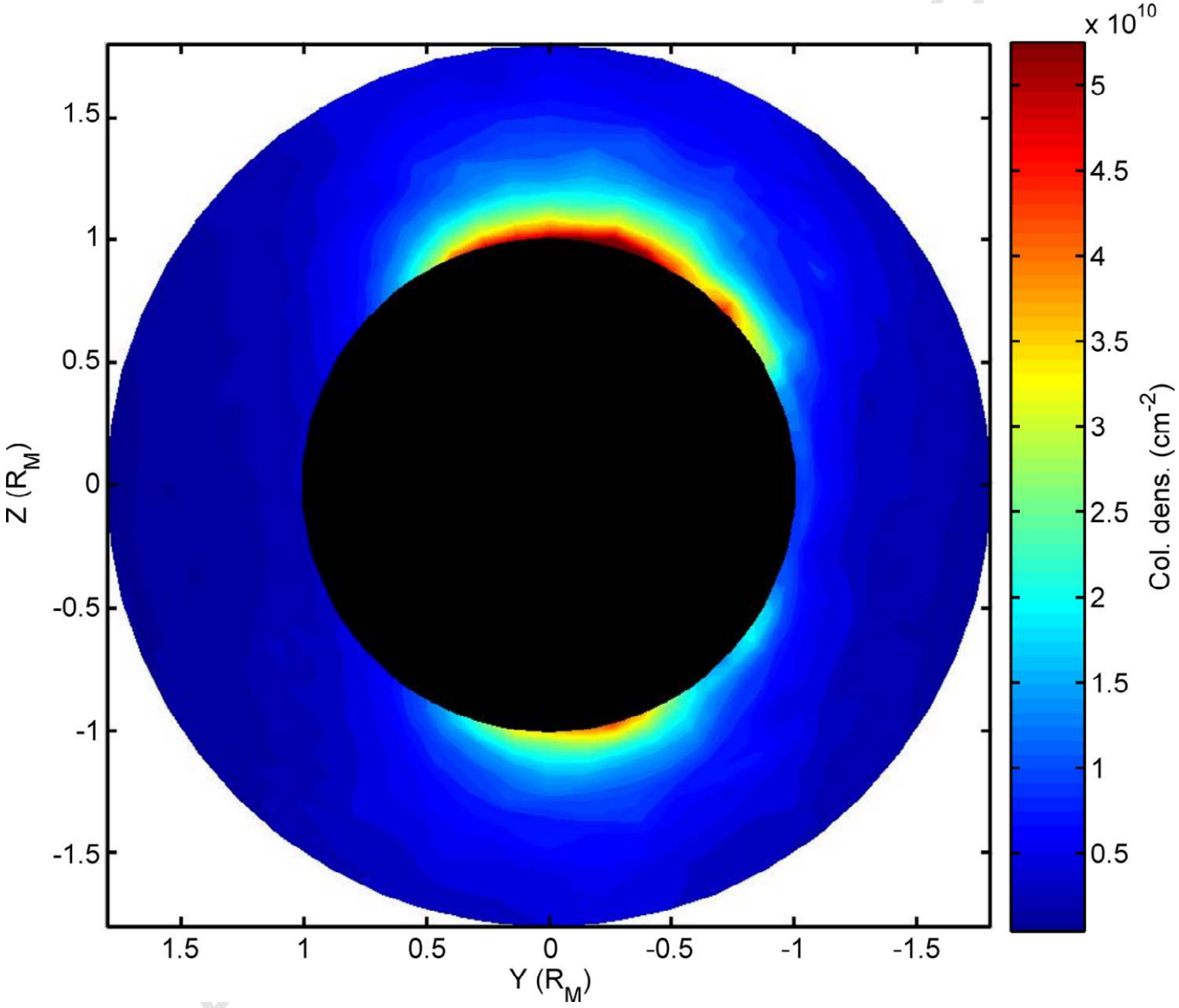

I10475-Fig5a

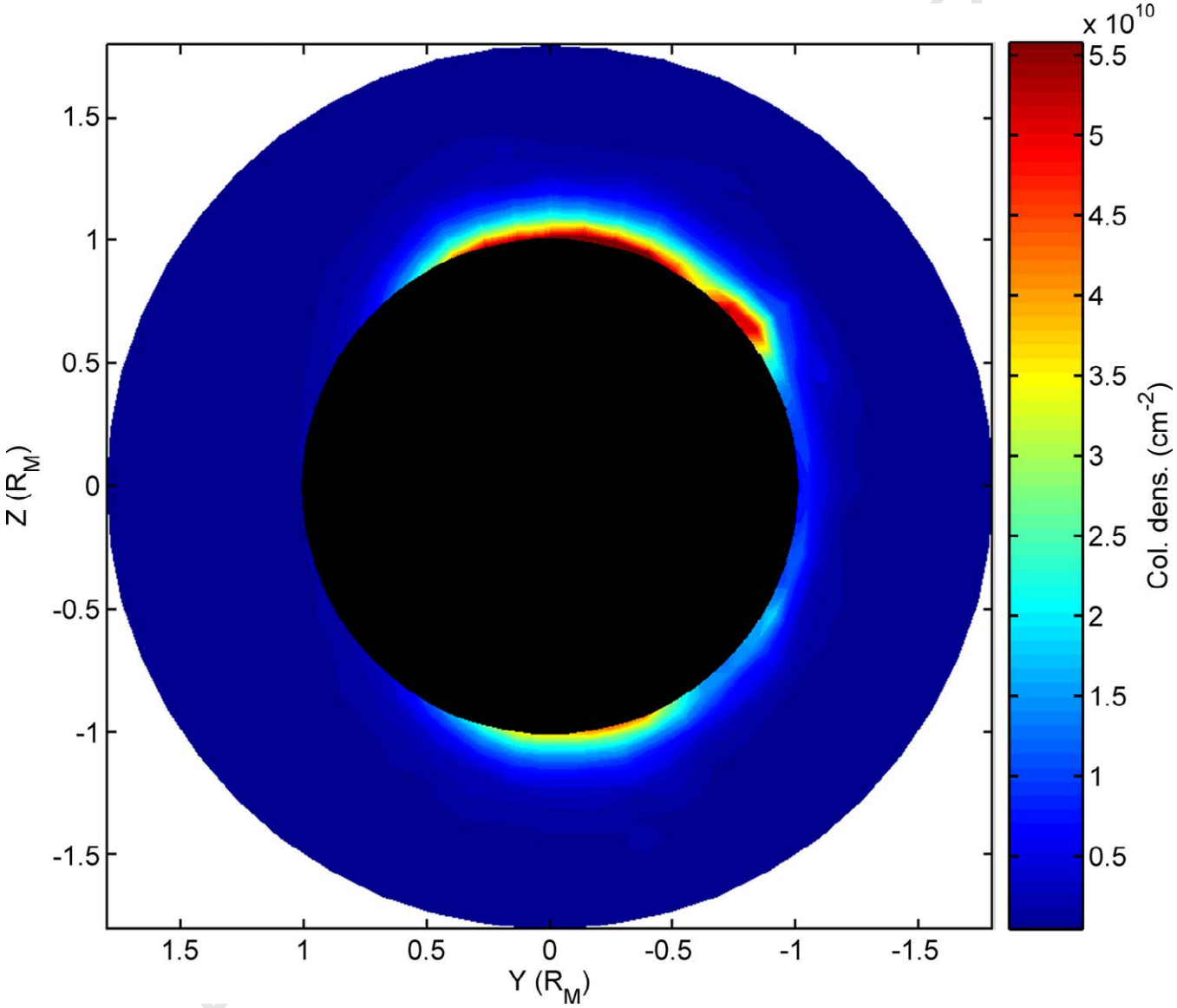

I10475-Fig5b

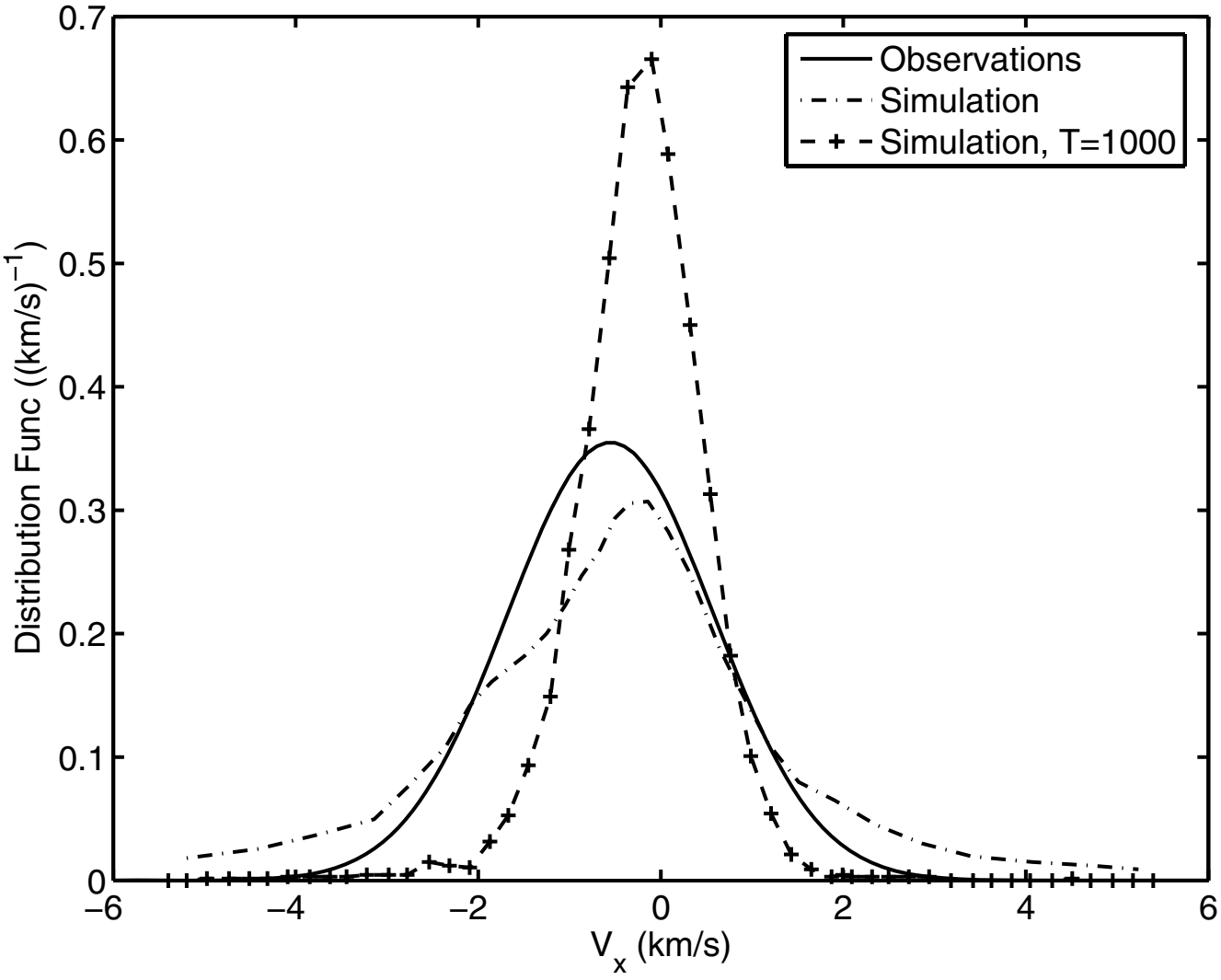

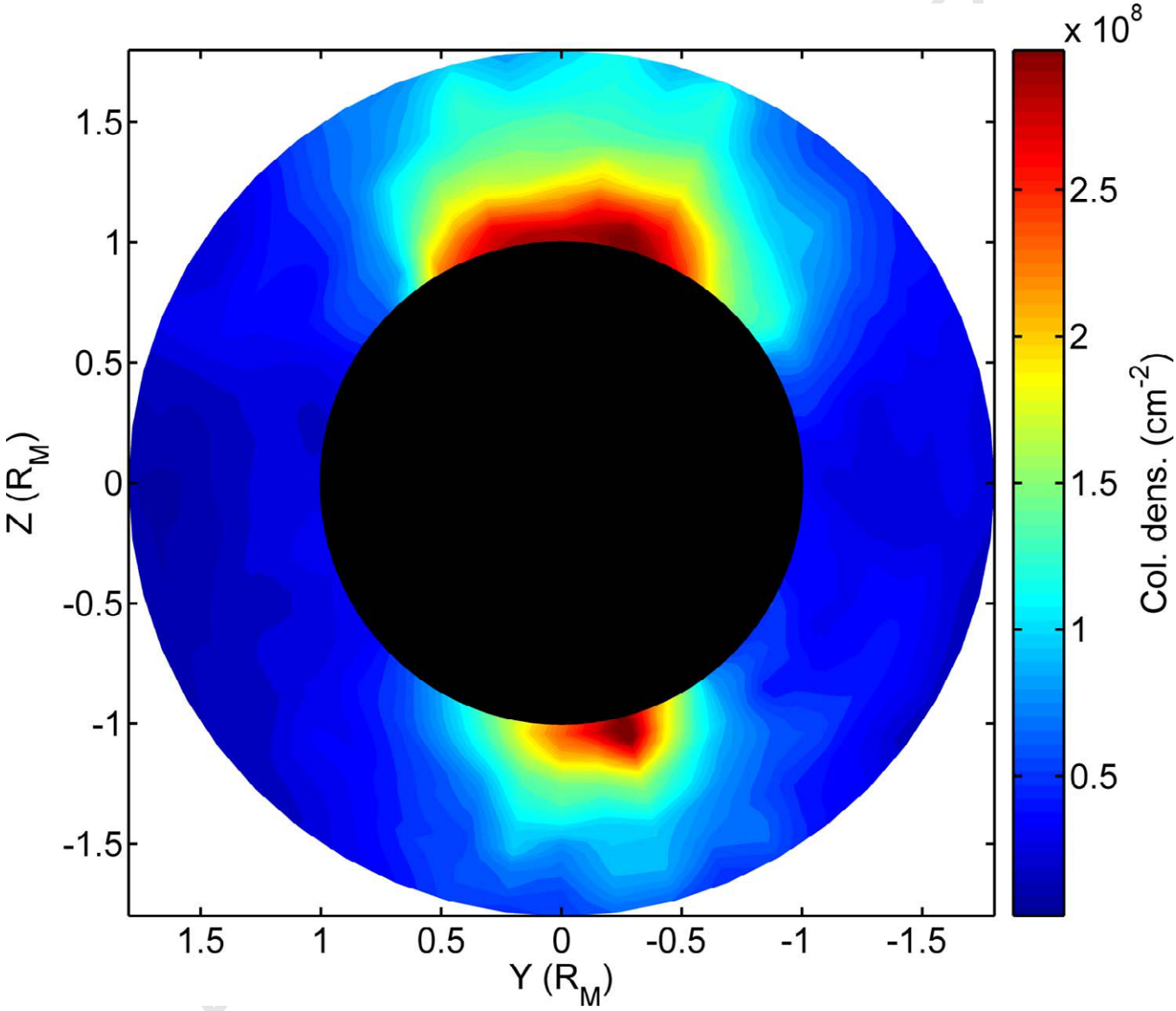

I10475-Fig7a

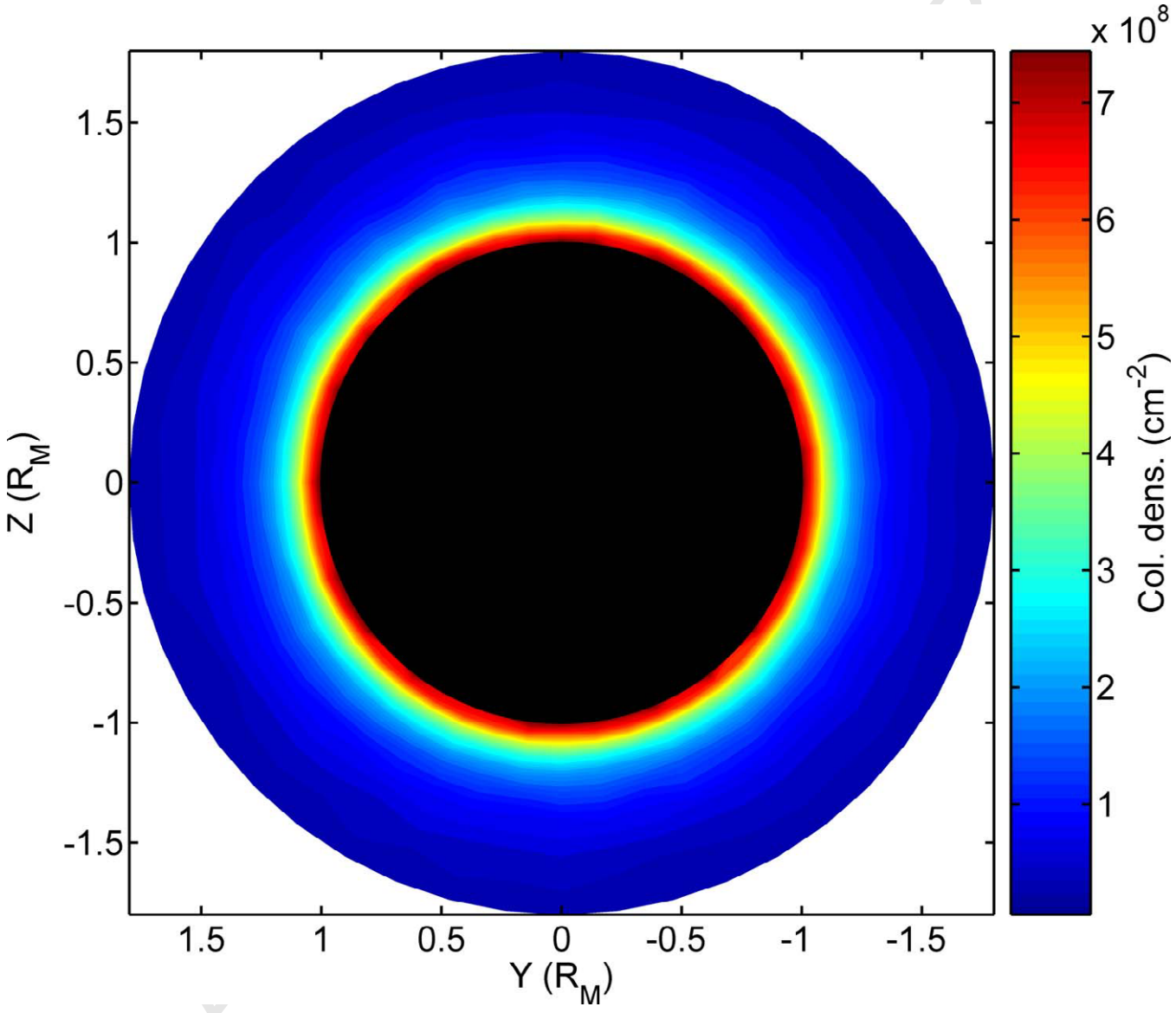

I10475-Fig7b